ADVANCED FUNCTIONAL MATERIALS
www.afm-journal.de

Conformal Self-Powered Inertial Displacement Sensor with Geometric Optimization for In Situ Noninvasive Data Acquisition

Yan Du, Penghui Shen, Houfang Liu, Zhiwei Zhang, Tianling Ren, Rui Shi, Zhonglin Wang, and Di Wei**

The growing focus on health management and smart technology advancements have propelled the use of wearable sensors in healthcare and human body motion analysis, particularly in preventing work-related upper limb musculoskeletal disorders (MSDs) through guided exercises. However, most available wearable medical sensors are rigid, bulky, and incapable of in situ recognition of the comprehensive motion of human body. Here, a conformal self-powered inertial displacement sensor (CSIDS) with geometric optimization for in situ noninvasive inertial data acquisition is proposed. Leveraging template-assisted processing and COMSOL simulation, the geometric configurations of tribo-layer materials, specifically focusing on the curvature of semicylindrical protrusions is systematically altered. This enhancement significantly improves the detection accuracy of joint range of motion. The features of shoulder joint bending angles and linear accelerations of the humerus are accurately captured using a deep learning model based on multilayer perceptron (MLP) networks, resulting in an exceptional recognition accuracy of 99.38% and 99.58%. Compared to traditional TENG wearable sensors that can only identify single metrics, CSIDS achieves a more comprehensive health assessment through inertial data detection. This system provides early warning for shoulder joint diseases, prevents MSDs, and extends to smart wearables for comprehensive joint health and ergonomic monitoring.

1. Introduction

In recent years, wearable sensors have garnered significant attention in the fields of healthcare and human motion analysis due to their potential for in situ monitoring of physiological parameters and movements. Work-related musculoskeletal disorders (MSDs) involving the upper limb have garnered significant attention due to their adverse impact on individual health and socio-economic implications.[1] These disorders may lead to decreased quality of life, increased risk of developing rheumatoid arthritis, and diminished work efficiency. Among these, athletes engaged in upper limb activities face an elevated risk of shoulder joint injuries, prevalent in sports requiring frequent upper limb usage, such as tennis, basketball, and volleyball. Shoulder joint injuries have been reported as one of the most common symptoms among MSDs patients, accounting for ≈25% of reported cases.[2] Hence, there is an urgent need to develop a monitoring system capable of continuously

Y. Du, Z. Zhang, Z. Wang, D. Wei
Beijing Institute of Nanoenergy and Nanosystems
Chinese Academy of Sciences
Beijing 101400, P. R. China
E-mail: zhong.wang@mse.gatech.edu; dw344@cam.ac.uk
Y. Du, Z. Zhang
School of Nanoscience and Engineering
University of Chinese Academy of Sciences
Beijing 100049, P. R. China
P. Shen, H. Liu, T. Ren
School of Integrated Circuits & Beijing National Research Center for Information Science and Technology
Tsinghua University
Beijing 10084, P. R. China
R. Shi
National Center for Orthopaedics
Beijing Jishuitan Hospital
Beijing Research Institute of Traumatology and Orthopaedics
Capital Medical University
Beijing 102200, P. R. China
Z. Wang
Beijing Key Laboratory of Micro-Nano Energy and Sensor
Center for High-Entropy Energy and Systems
Beijing Institute of Nanoenergy and Nanosystems
Chinese Academy of Sciences
Beijing 101400, P. R. China
Z. Wang
Guangzhou Institute of Blue Energy, Knowledge City
Huangpu District, Guangzhou 510555, P. R. China
Z. Wang
Georgia Institute of Technology
Atlanta, GA 30332-0245, USA

The ORCID identification number(s) for the author(s) of this article can be found under https://doi.org/10.1002/adfm.202409602

DOI: 10.1002/adfm.202409602

tracking joint movements during daily activities to prevent and rehabilitate upper limb MSDs. Although various monitoring systems have been proposed to capture motion signals from joints such as the wrist, knee, and ankle, primarily utilizing wearable sensors including inertial sensors (such as accelerometers[3] and gyroscopes[4]), strain gauges,[5] and optical fiber sensors,[6] most current systems encounter various limitations. These limitations comprise complex and rigid sensor structures, demanding data processing needs, high circuit energy consumption, and inadequate acquisition of motion information, thus constraining their effectiveness in practical applications.

The rapid development of flexible electronics technology has facilitated the application of wearable medical sensors in the monitoring of physiological information, including human movement,[7] body temperature,[8] heart rate,[9] and respiration.[10] By integrating conformal electronic sensors with the human skin, the scope of applications for monitoring various biological signals and body movements has been expanded. As a type of conformal sensor, pressure sensors account for a large proportion. Depending on the sensing element and mechanism, it can be divided into resistive,[11] capacitive,[12] piezoelectric,[13] and optical types.[14] Flexible pressure sensors, which convert mechanical stimuli from human movement-induced displacement and force inertia into electrical signal, are considered a promising choice for monitoring physiological information.[15] However, the complexity of shoulder movement renders existing flexible piezoelectric sensors insufficient to meet monitoring requirements due to their lack of stretchability and inertial detection capabilities, as well as the absence of real-time monitoring energy supply. Simultaneously, triboelectric nanogenerator (TENG) have gained widespread attention as an emerging technology in healthcare and the Internet of Things (IoT). TENGs provide robust power output and introduce self-powered sensing mechanisms such as vibration, human motion energy harvesting,[16] pressure sensing,[17] and information transmission.[18] Meanwhile, the geometric configurations of the tribo-layer materials plays a crucial role in optimising the performance of TENG sensors. Recent studies indicate that adjusting the geometric parameters of the electrodes can significantly affect the sensitivity, response time and detection accuracy of the sensor, thereby improving its performance in specific sensing applications.[19] Therefore, in addition to designing flexible and stretchable sensor structures,[20] further optimization and application expansion of TENG sensing technology can be achieved by carefully designing the geometric configurations of tribo-layer materials to meet the requirements of specific applications.

Herein, we propose a conformal self-powered inertial displacement sensor (CSIDS) with geometric optimization for in-situ noninvasive inertial data acquisition. Leveraging template-assisted processing and COMSOL simulation, we have identified that geometric configurations play pivotal role in monitoring human body sensing applications. The essential of the CSIDS lies in its utilization of tribo-layer materials featuring micro-patterned semicylindrical structures. The curvature of the semicylindrical configuration maximizes contact surface area, improving CSIDS signals and facilitating better monitoring of joint range of motion compared to other configurations. These findings emphasize the vital role of geometric configurations in tribo-layer materials for optimizing the sensing capabilities of TENG-based motion sensors. Furthermore, the introduction of a layer of carbon doped Ecoflex between the CSIDS and the skin will significantly reduce the impact of the human skin's strong positive potential. By integrating a deep learning model based on Multilayer Perceptron (MLP) networks, which can accurately capture the features of shoulder joint bending angles and linear accelerations of the humerus. The average accuracy can reach 99.38% and 99.58%. Additionally, due to the excellent ductility of the CSIDS, it maintains a robust linear relationship between triboelectric signals and applied strain at 110%. The application of CSIDS was demonstrated in monitoring wrist joint and elbow joint motion. Compared to traditional TENG wearable sensors that can only identify single metrics,[21] CSIDS achieves a more comprehensive health assessment through inertial data detection. This lays the groundwork for early warning of shoulder joint diseases, prevention of MSDs, and establishment of a comprehensive joint health and ergonomic monitoring system.

2. Results and Discussion

2.1. The Structure Design of CSIDS

The CSIDS system is illustrated in **Figure 1a**. CSIDS were attached to the skin surface of the shoulder joint, elbow joint, and wrist joints to monitor joint motion and help to prevent upper limb MSDs. Joint motion caused the CSIDS to deform, converting them into electrical signals. The creation of this system was crucial in enhancing the precision and in situ capabilities of medical diagnostics. The 3D structure of CSIDS is shown in Figure 1b, where the main components were based on semicylindrical Ecoflex and carbon doped Ecoflex, which were firmly adhered to the Ecoflex base to facilitate contact separation. Ecoflex, widely used in the fields of biomedical engineering and wearable devices, was preferred due to its flexibility, stretchability, biocompatibility, and chemical stability. Furthermore, its high electronegativity made it the desired material for the tribo-layer and insulating layers of TENG. The conductive layer and shielding layer were built on a conductive composite material of carbon black infiltrating network and Ecoflex. Thanks to the strong interface bonding between carbon black and the Ecoflex matrix, this material exhibited good electrical properties Additionally, Ecoflex exhibits high flexibility and comfort, effectively adapting to the bending and stretching of human skin, thereby avoiding discomfort caused by material rigidity.[22] Moreover, the performance of TENG sensors was susceptible to the influence of the contact surface, and the micro-topological structure on the tribo-layer surface could increase the contact area and thereby enhance performance. To seek a convenient and cost-effective method for manufacturing Ecoflex topological structures, we adopted 3D printing technology to shape Ecoflex with prominent vertical stripes (Figure 1c(i)). As shown in Figure S1 (Supporting Information),

D. Wei
Centre for Photonic Devices and Sensors
University of Cambridge
9 JJ Thomson Avenue, Cambridge CB3 0FA, UK

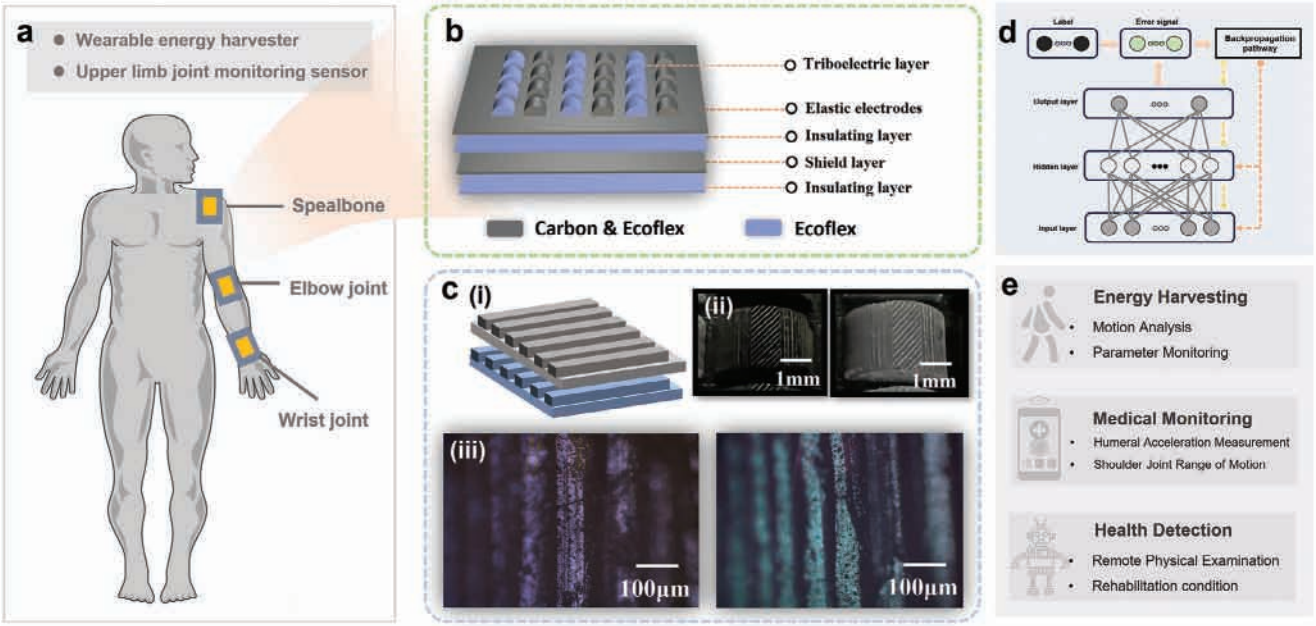

Figure 1. Schematic representation of CSIDS for assessing the functionality of the human upper limb joints. a) CSIDS can be attached to the joints of the human upper limb for in situ monitoring. b) 3D structural representation of CSIDS. c) Surface microstructure of carbon-doped Ecoflex and Ecoflex materials: i) Schematic representation of the 3D structure; ii) and iii) Optical microscope images of carbon-silicone and silicone-based materials. d) Data processing framework based on machine learning. e) Noninvasive monitoring provides access to human information.

this method involved constructing a semicylindrical mold using 3D modeling software, followed by 3D printing with polylactic acid (PLA). During the process of hot melt extrusion, PLA formed a textured structure of surface stripes. Subsequently, we mixed Ecoflex materials A and B and poured them into the 3D mold to achieve the initial preparation of CSIDS. After the Ecoflex semi-solidified, we filled the residual part of the mold with carbon doped Ecoflex to form the main structure of CSIDS. The energy spectrum analysis (Figure S2, Supporting Information) showed the composition of the carbon doped Ecoflex. Based on this, we further deposited Ecoflex and carbon doped Ecoflex to form the insulating layer and shielding layer. Finally, the mold was placed in a vacuum oven for drying. After 5 hours, the CSIDS could be carefully peeled off.

The parameters of CSIDS were shown in Figure S3 (Supporting Information). The photograph of the CSIDS is shown in Figure S4 (Supporting Information). Optical microscope images of the textured surface of the Ecoflex are displayed in Figure 1c(ii) and Figure 1c(iii). Additionally, Figure 1d demonstrates a MLP networks model used for classifying joint movements, which could provide strong support for medical diagnostics, motion analysis, rehabilitation therapy, and other fields, bringing new breakthroughs and advancements to human health and exercise science research. Figure 1e illustrates the application prospects of noninvasive monitoring of CSIDS for accessing human body information. By means of self-powered sensing capability, we are poised to realize automated in situ measurement of upper limb and even medical remote follow-up. This pioneering advancement holds the potential to exert a profound influence on the domains of healthcare and human body motion analysis.

2.2. Working Mechanism of Geometric Optimization of CSIDS

The geometric configurations of tribo-layer materials exerted a substantial influence on sensor performance. To attain a comprehensive understanding of the effects of these geometric configurations on the output performance of CSIDS, 3D printing technology was employed to manufacture three distinct geometric configurations (cube, triangular prism, and semicylinder) of molds. The diverse geometric configurations displayed distinct contact states under simulated real-world usage conditions. Upon observation and analysis, it was found that the cube configuration demonstrated line-to-line contact, whereas the triangular configuration exhibited face-to-face contact. In contrast, owing to its curvature characteristics, the semicylinder configuration showcased a more comprehensive contact state (**Figure 2a**). These disparate contact states directly impacted the deformation of the triboelectric materials and the generation of electrical signals, consequently influencing the output performance of CSIDS.

The working principle of CSIDS with different geometric configurations and COMSOL simulations based on finite element analysis is shown in Figure 2b,c. In the CSIDS system, due to multiple contact and separation cycles between carbon doped Ecoflex and Ecoflex, the carbon doped Ecoflex carried positive charges while the Ecoflex carried negative charges (State I). This charge distribution was caused by surface charge transfer due to contact-separation cycles. Joint movements exerted pressure on CSIDS, causing it to bend. During the bending process, electrons flowed from carbon doped Ecoflex to the ground through an external circuit to maintain static equilibrium (State II). When the distance between carbon doped

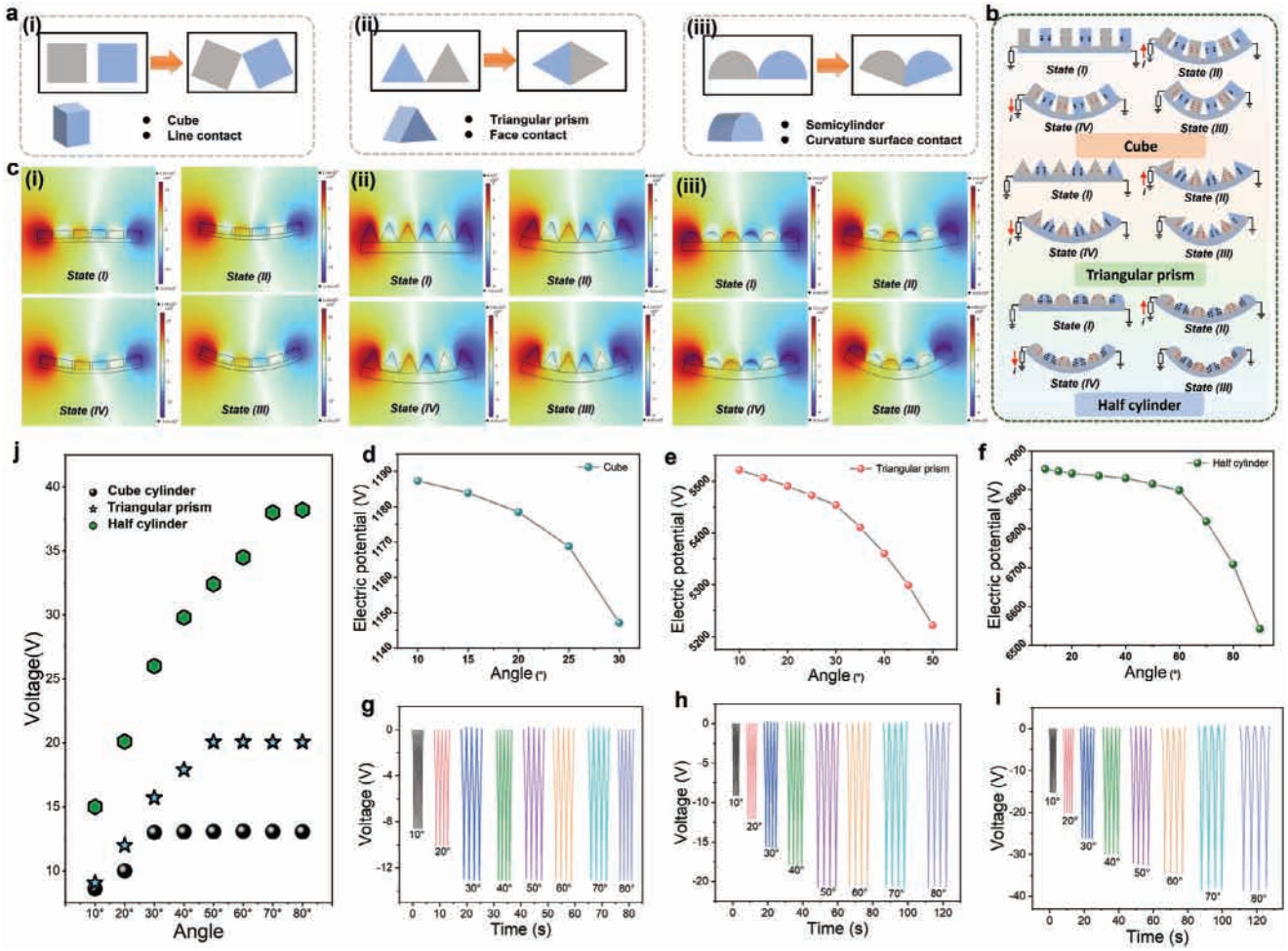

Figure 2. Working principle of CSIDS under different geometric configuration and theoretical simulation and experimental verification. a) Contact state of CSIDS under different geometric conFigureuration. b) Schematic of the working principle of CSIDS under different geometric conFigureuration. c) COMSOL potential simulation of CSIDS under different geometric conFigureuration. d,e) Simulation of the behavior of CSIDS with different geometric configuration using the finite element method. g–i) Output performance of CSIDS with different geometric configuration at different bending angles. j) Comparison of the output performance of CSIDS with different geometric configuration at different bending angles.2.3 Parameter Optimization and Output Performance Evaluation of CSIDS.

Ecoflex and Ecoflex was minimal (State III), the potential difference between them was minimized. During the bending recovery process, electrons flowed from the ground to carbon doped Ecoflex through an external circuit to maintain static equilibrium (State IV). This series of processes formed a complete cycle of charge generation. We performed comprehensive theoretical simulations (Figure 2d–f) utilizing finite element methods for CSIDS featuring various configurations, with performance characterized by the potential curve on the Ecoflex surface. Simulation outcomes revealed that when the base of CSIDS was semicylindrical, its signal capture capability was enhanced, likely attributed to its more efficient contact area and geometric characteristics. Subsequently, we demonstrated the output performance of CSIDS with different geometric configurations at varying bending angles in Figure 2g–i. Additionally, we calculated the theoretical maximum contact areas for CSIDS with different geometric configurations. The contact area of the half-cylinder structure was found to be 1.65 times greater than that of the cubic structure and 3.809 times greater than that of the triangular prism structure (Note S1, Supporting Information). It was worth noting that soft contact materials can absorb and disperse stresses through their own deformation when subjected to external mechanical forces, and CSIDS with different geometrical configurations works in the expected strain range to ensure that the elastic limit of the material is not exceeded. Ensuring operation within the intended strain range was critical for maintaining the stability of triboelectric signals. The CSIDS maintained its performance within the material's elastic limits during practical use due to its optimized geometric design and material choices, ensuring both signal stability and sensor reliability. Design considerations included experimental and analytical determination of the material's safe strain range and optimization of structure and performance within this range to guarantee long-term stability in practical applications. By comparing the performance of CSIDS with different geometric configurations in Figure 2j, a relationship between signal response and bending angle was

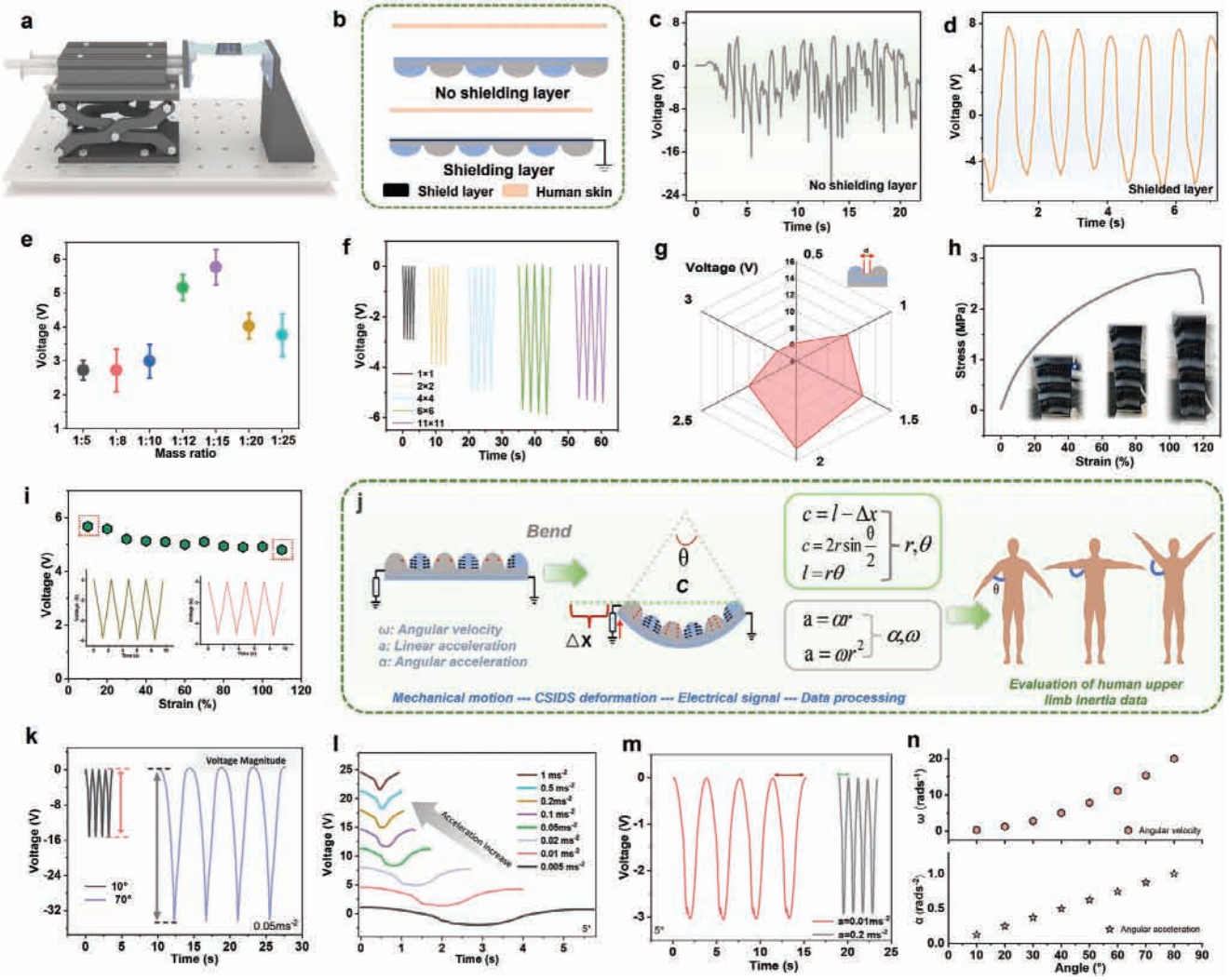

Figure 3. Parameter optimization and output performance of CSIDS under joint motion simulation. a) Experimental platform for simulating human joint motion. b) Schematic diagram of CSIDS with and without shielding. c) Output signal of CSIDS without shielding layer. d) Output signal of CSIDS with shielding layer. e) Performance exploration of CSIDS under different Ecoflex-carbon mass ratios. f) Output performance of CSIDS with different array numbers under the same area. g) Output performance of CSIDS with different gap of Ecoflex-based materials. h) Stress–strain curve of CSIDS. i) Output performance of CSIDS under tensile conditions. j) Schematic representation of the inertial parameters that can be deduced from the motion simulation of the CSIDS. k) Feedback characteristics exhibited by the voltage amplitude of the CSIDS at different bending angles. l) Output performance of CSIDS under different linear accelerations. m) Feedback characteristics of CSIDS exhibited by voltage amplitude under different linear accelerations. n) Derived angular acceleration and angular velocity of CSIDS under different bending angles.

observed, particularly when the base of CSIDS was semicylindrical, consistent with our simulation results. The superior output performance of the semicylindrical base CSIDS is demonstrated in Figure S5 (Supporting Information). These findings contributed to a deeper understanding of the performance characteristics of CSIDS and provided important insights. In summary, while the bending angle positively correlated with voltage output when other parameters were constant, this relationship was influenced by factors such as contact area, contact pressure, dynamic triboelectric behavior, and environmental conditions. Although the bending angle significantly impacted voltage output, the overall voltage resulted from the interplay of material properties, geometric configurations, and other contributing factors.

2.3. Parameter Optimization and Output Performance Evaluation of CSIDS

Figure 3a and Figure S6 (Supporting Information) depict the experimental setup constructed using a linear motor to simulate human joint movements (Movie S1, Supporting Information). A schematic of the structure of the CSIDS with and without a shield is shown in Figure 3b. As a wearable device, mitigating the strong influence of skin potential on CSIDS was crucial. To validate this point, a comparative experiment was conducted. The operation of CSIDS without a shielding layer was initially studied. Subsequently, the formation of a single-electrode mode TENG between the joint skin and the CSIDS was identified. This TENG induced additional charges, which impeded the output signal of CSIDS,

consequently impacting its performance (Figure 3c). To address this issue, a shielding layer was introduced, serving as a protective shell to isolate the potential between CSIDS and human skin. Meanwhile, the human body serves as a charge reservoir, providing or storing charges for the shielding layer. This design effectively reduces interference from CSIDS to the skin, as demonstrated in Figure 3d, where the performance of CSIDS was notably enhanced. According to Figure 3c, CSIDS without a shielding layer exhibits a complex signal rather than a single pulse representing the bending state. To verify the interference of joint skin potential on CSIDS, additional tests were conducted using a simple device, as shown in Figure S7c (Supporting Information). It followed the contact-separation model of TENG shown in Figure S7a (Supporting Information). This further underscores the importance of the shielding layer for the CSIDS system, particularly in reducing external interference and improving system performance.

Another factor influencing the output signal is the mass ratio of Ecoflex to carbon powder. As illustrated in Figure 3e, the output voltage increases as the mass ratio of Ecoflex to carbon shifts from 1:5 to 1:15. This was attributed to the increased electron mobility with higher carbon doping concentrations. However, when the mass ratio shifts from 1:15 to 1:25, the output voltage decreases due to the adverse effect of excessively high carbon doping concentrations. Cross-sectional SEM images of carbon/Ecoflex composites with varying mass ratios revealed that the number of carbon bundles increased with higher carbon black content. This is due to the fact that the interfacial properties of the tribo-layer play an essential role in the improvement of the TENG performance, and therefore the exposure of carbon at the interface affects the output voltage (Figure S8, Supporting Information). Therefore, the optimal mass ratio of Ecoflex to carbon was determined to be 1:15. Additionally, a controlled variable method was employed to assess the impact of different sizes of semicylindrical CSIDS on output performance. In this experiment, the spacing "d" between the conductive semicylinders and the insulating semicylinders was fixed at 1 mm. Different numbers of semicylindrical molds were designed under the same template size (50 mm × 70 mm). As shown in Figure S9 (Supporting Information), the length of the semicylinder equals the diameter "D" of the semicircle cross section, and the height equals the radius "R" of the semicircle cross section. Since the length and width of the template were fixed, the width of the semicylinder varies with the diameter "D." As depicted in Figure 3f, the output signal increased with the increasing length "D" of the semicylinder. This might be due to the increase in the number of paralleled TENG as the array number increases. When the length and width of the semicylinder were 7.2 mm × 10.5 mm, optimal performance was achieved. However, when the length and width were 3.9 mm × 6.9 mm, a certain degree of signal decline was observed. This was because although the increase in the number of arrays increases the number of TENG, it simultaneously reduced the contact area between the Ecoflex and carbon doped Ecoflex, resulting in a reduction in the signal to some extent. In summary, the semicylindrical geometry and its ordered arrangement provided significant performance advantages in CSIDS design. The size, shape, and distribution of the semicylindrical will lead to different results. Selecting the appropriate size and arrangement was key to optimizing CSIDS performance, while other shapes, such as elliptical cylinders, faced challenges in design complexity and performance stability.

Figure 3g illustrates the influence of the spacing "d" between the conductive semicylinders and the insulating semicylinders on the performance of CSIDS. The optimal semicylinder array of dimensions 10.5 mm × 7.2 mm × 5.25 mm was selected. Explorations were conducted with spacings of 0.5, 1, 1.5, 2, 2.5, and 3 mm (Figure S10, Supporting Information). The results indicated that a spacing of 2 mm yields optimal performance. This might be due to the fact that excessively large spacings impeded the effective contact between the semicylinders and the insulating semicylinders, while excessively small spacings affect the contact-separation distance of TENG, thereby influencing voltage signals. Additionally, Figure S11 (Supporting Information) demonstrates the output performance of Ecoflex and carbon doped Ecoflex materials under different arrays. An increase in the logarithm results in a greater number of parallel TENG units, which in turn leads to enhanced performance. Furthermore, both the current and charge characteristic of CSIDS are also shown in Figure S12 (Supporting Information). Figure 3h illustrates the stress–strain curve of CSIDS, demonstrating a good linear relationship between the triboelectric electrical signal and the impact force at 110% strain. Additionally, the triboelectric signal of CSIDS remained relatively stable under different stretching ratios, with minimal voltage fluctuations (Figure 3i). The output performance of CSIDS at different humidity levels was shown in Figure S13 (Supporting Information). The results demonstrated that the signal output of the sensor decreased as the humidity increased. This occurred because the surface of the friction material absorbed moisture, and in high humidity environments, the surface charge could be carried away by the moisture, leading to changes in the charge transfer characteristics and affecting the signal strength. Although humidity could have a detrimental effect, typical medical monitoring environments maintained moderate humidity levels, which generally did not significantly affect the sensor's performance. Consequently, CSIDS remained capable of providing stable and reliable signals under such conditions, fulfilling the requirements for medical monitoring applications. The output voltage of the CSIDS under different dielectric thicknesses is shown in Figure S14 (Supporting Information). As the dielectric thickness increased, the output signal significantly decreased. This was primarily due to the weakening of the capacitive effect caused by the increased thickness, which in turn affected the charge transfer efficiency. Conversely, the output voltage of the CSIDS under different contact areas is shown in Figure S15 (Supporting Information). As the contact area increased, the output signal significantly enhanced. This was due to the increased contact efficiency, leading to a higher amount of charge transfer. A larger contact area could more effectively capture triboelectric signals, thereby increasing the output voltage. CSIDS has a wide sensing range for both shoulder joint bending angles and material strain. It can monitor shoulder joint angles from 0° to 90°, making it suitable for various shoulder joint motions. Additionally, the sensor supports a strain range of up to 110%, allowing it to accommodate a broad spectrum of material strains. In terms of sensitivity, CSIDS exhibits a bending angle sensitivity of 0.33 V/degree and a strain sensitivity of 0.0079 V/%, ensuring accurate responses to joint

motion and strain changes (Note S2, Supporting Information). The inertial parameters derived from the simulated motion of CSIDS are shown in Figure 3j. A series of inertial parameters (angle, angular velocity, angular acceleration) can be derived from the above formula through the known parameters, for example, the distance of the linear electrode movement (ΔX) and linear acceleration (a). As the joint moves, the CSIDS deforms, identifying inertial data through the distinct electrical signals generated. This was attributed to soft contact effectively reducing potential wear and damage during sensor usage, thereby extending its lifespan. Figure 3k showcases the feedback characteristics of voltage amplitude of CSIDS under different bending angles. Figure 3l displays the output signal under different linear accelerations. Increasing linear accelerations resulted in a more compact waveform in the time domain. Figure 3m illustrates the feedback characteristics of waveform time span of CSIDS under different linear accelerations. The derived angular acceleration and angular velocity of CSIDS at different bending angles are shown in Figure 3n, and the specific parameters are shown in Table S1 (Supporting Information). This indicates that CSIDS can effectively monitor the bending angular velocity of the shoulder joint, measure the linear accelerations of the humerus, and derive additional inertial parameters. Through these experimental validations, we further demonstrate the reliability and accuracy of the sensor in medical monitoring applications, providing reliable technical support for its extensive application in healthcare.

2.4. Machine Learning–based Data Processing

While the structural parameters of CSIDS have been optimized and the output signal characteristics for linear acceleration and bending angle recognition are evident, traditional approaches struggle to achieve high recognition accuracy due to the complexity of real-world environments. With the rapid development of artificial intelligence, machine learning, especially deep learning, has received extensive attention. To eliminate baseline drift errors in CSIDS, we conducted a series of preprocessing operations on the linear accelerations data for deep learning algrithm. The multilayer perceptron (MLP) algorithm was chosen due to its robust nonlinear fitting capability, ability to handle high-dimensional data, flexibility in classification and regression tasks, and well-established training and optimization mechanisms. These attributes enabled MLP to effectively process the complex data collected by CSIDS, thereby improving the prediction and classification accuracy of the sensor performance. Initially, we employed a linear interpolation method to fill in missing values, ensuring data integrity. Subsequently, the interpolated data were resampled to the specified target frequency for subsequent analysis and model training. To eliminate potential linear trend effects, we implemented linear trend removal on the resampled data using function subtraction. Because the frequency differences in linear acceleration data are significant, for better classification, we extracted and transformed features from the preprocessed data into spectrogram format, achieved through the fast Fourier transform algorithm (Figures S16 and S17, Supporting Information). In the processing of angle of bend data, we adopted a similar processing flow and neural network architecture as for linear accelerations, with the difference being that we did not extract frequency features from the preprocessed data; instead, we normalized the data to ensure that the distribution range of samples is more suitable for neural network computation. In terms of dataset construction and model structure, we employed methods consistent with those described above.

Furthermore, we truncated the generated spectrograms to reduce data dimensions and improve computational efficiency. To meet the requirements of multi-classification tasks, we converted the original labels into one-hot encoding format and constructed a dataset containing the transformed spectrogram features and corresponding one-hot encoding labels. Subsequently, the dataset was randomly divided into training and testing sets at a ratio of 4:1 using a random method, used for model training and performance verification, respectively (**Figure** 4a,b). To extract effective features from the data and accomplish classification tasks, we employed the backpropagation (BP) neural network algorithm with MLP structure consisting of input, hidden, and output layers (Figure 4c). The size of the input layer depends on the spectrogram features after preprocessing, while the hidden layer is set to a specific number (in this case, 30 neurons), and the size of the output layer matches the dimension of the one-hot encoding labels. Through the backpropagation algorithm, the network can update the weight parameters of each layer from bottom to top based on the error between the actual prediction results and the true labels, continuously optimizing the model performance. BP neural networks can capture nonlinear relationships in the data and exhibit good fitting capabilities for many complex classification tasks.

During training, we selected the cross-entropy loss function as the optimization objective and employed the Adam optimization algorithm to dynamically adjust model parameters. Over multiple training epochs (10 epochs), the model performed forward propagation to calculate prediction results for each batch of data in the training set and updated model parameters through backpropagation to compute gradients. Throughout this process, we recorded the average loss for each training epoch. After completing each training epoch, we evaluated the model's performance on an independent testing set, recording key evaluation metrics such as accuracy (Figure 4d,e). After 10 rounds of training, the linear accelerations test results showed an overall accuracy of 99.58% (Figure 4f). In terms of the construction of the bending angle dataset and model structure, we followed the same approach as described above. The only difference is the expansion of input dimensions, for which we directly adjusted the number of neurons in the hidden layer (60 neurons) and the number of training rounds (30 rounds). The final test results showed an accuracy of 99.38% (Figure 4g). The detailed description of the confusion matrix is shown in Note S3 (Supporting Information). Through the aforementioned computational processes, we demonstrated that the data collected by our sensor possess significant discriminative power. With simple algorithmic coordination, experimental data can be automatically preprocessed and classified, providing further support for the future application prospects of the sensor.

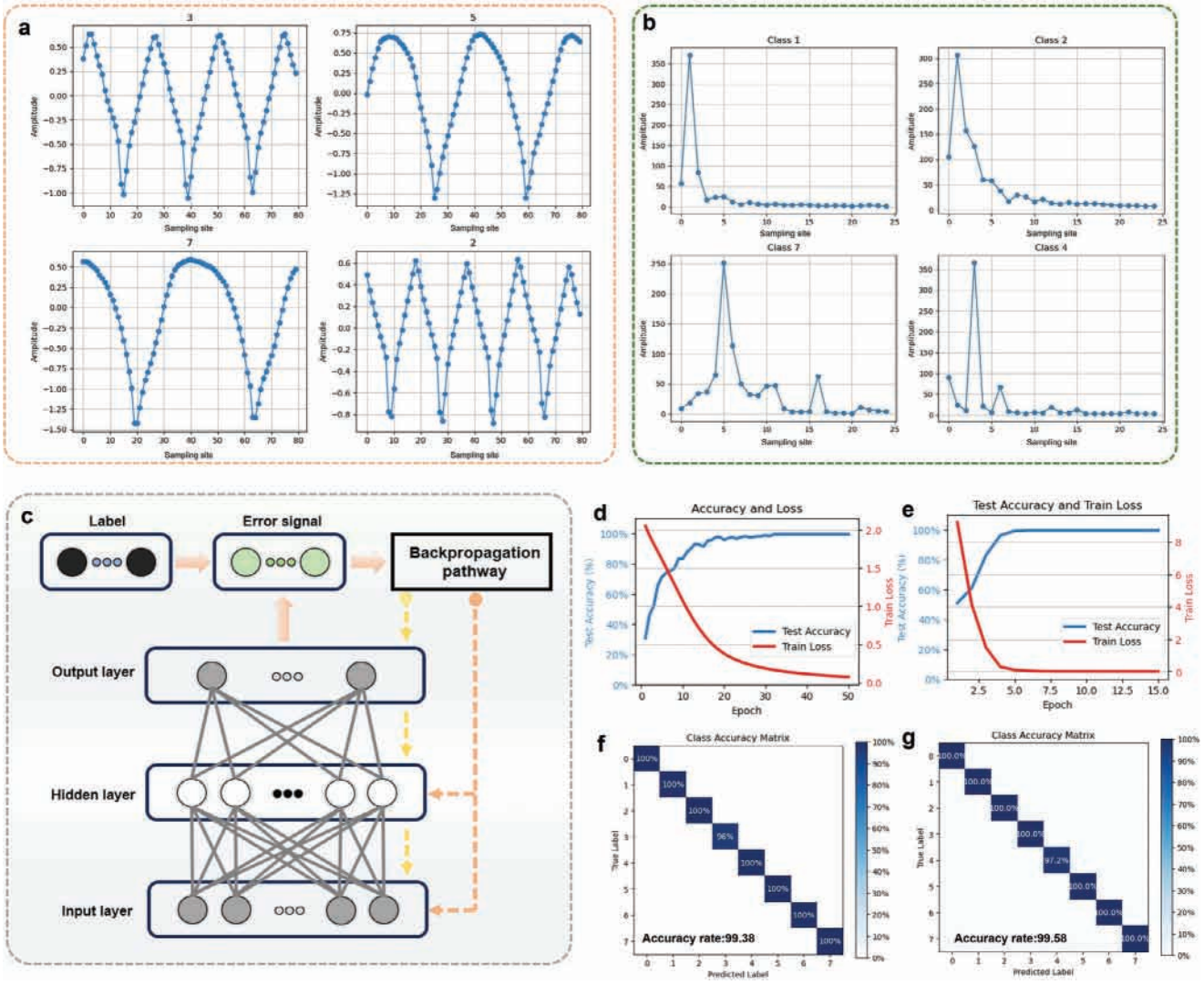

Figure 4. Machine learning based data processing. a) Data preprocessing (linear acceleration – frequency spectrum spectrum). b) Data preprocessing (bending angle – frequency spectrum spectrum). c) Structure of neural networks (network structure, back propagation). d) Training process (linear acceleration). e) Training process (bending angle). f) Training result display (linear acceleration). g) Training result display (bending angle).

2.5. The Application of CSIDS in Monitoring Human Body Information

The shoulder joint was one of the most complex joints in the human body, involving a wide range of motion and the coordinated action of multiple muscles and ligaments. The scapula, as a crucial component of the shoulder joint, played a vital role in its normal function.

However, for upper limb athletes, disorders in scapular motion could lead to the loss of shoulder joint function, often manifested as the inability to lift the arm or other restricted movements (**Figure 5**a). Therefore, timely and accurate monitoring of shoulder joint activity was of paramount importance for diagnosing and treating shoulder joint-related disorders (Figure 5b). A photograph of CSIDS applied to the human upper limb joint is displayed in Figure 5c. The CSIDS were installed on the shoulder joint to reflect its activity status (Figure 5d). When shoulder joint activity was restricted, the CSIDS contact was lighter, resulting in weaker output signals, manifested as positive or weakly positive. Conversely, when the shoulder joint moved normally, the CSIDS contact was more complete, resulting in stronger output signals, manifested as negative. Utilizing this, interface of shoulder joint signal indication system was developed (Figure 5e), where red indicates a positive signal, yellow denotes a weakly positive signal, and green signifies a negative signal (Movie S2, Supporting Information). This rapid and accurate monitoring method assisted healthcare professionals in taking timely therapeutic measures. Additionally, the CSIDS were affixed to the wrist joints (Figure 5f) and elbow joints (Figure 5g) of the human body (Movie S3, Supporting Information). CSIDS could precisely monitor bending changes by maintaining stable contact charge transfer and having a sensitive dynamic response capability, even when the human joint was at a fixed bending angle. Moreover, the CSIDS design considered both dynamic and static voltage output

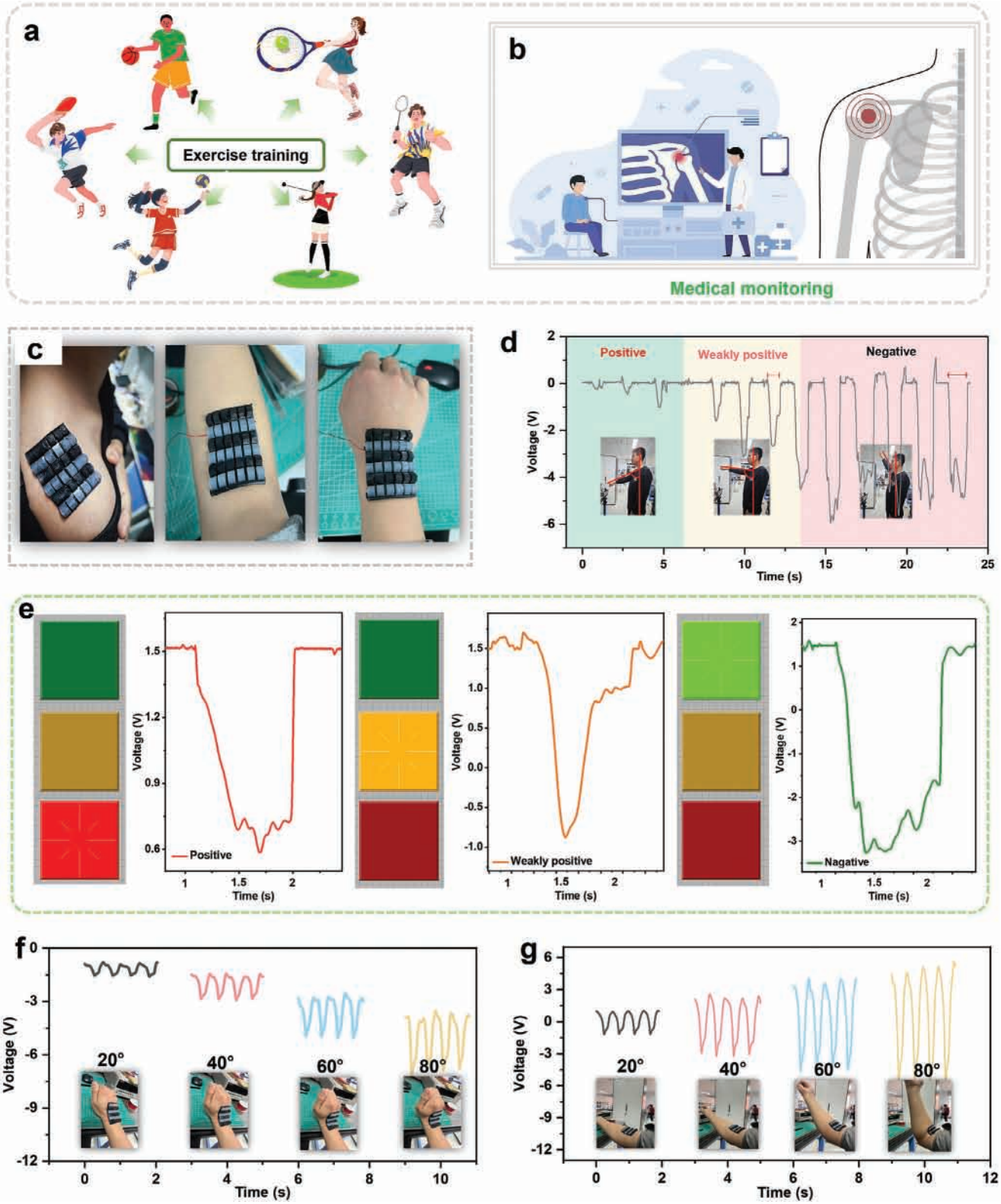

Figure 5. Application of noninvasive CSIDS in monitoring human information. a) Shoulder joint damage faced by upper limb athletes. b) Prospects of CSIDS application in monitoring human shoulder joints. c) Photograph of CSIDS attached to human joints. d) CSIDS diagnosing restricted range of motion in human shoulder joints. e) Interface of shoulder joint signal indication system. f,g) Application of CSIDS in monitoring wrist joints f) and elbow joints g).

characteristics. The AC signals generated by dynamic movement, when maintained at a certain angle, would stabilize due to the continued contact. Any minor movements could induce slight contact and separation, resulting in small AC signals. This characteristic endowed the CSIDS with high sensitivity and accuracy in monitoring elbow angle variations during writing. (Figure S18, Supporting Information). By monitoring the signal amplitude variation produced by the sensors under different degrees of bending, further insights into limb activity could be gained. This CSIDS-based method for monitoring the human body, with human joints serving as the entry point for medical IoT applications, underscores its vast potential in healthcare and human motion analysis fields. It presents a new paradigm for future medical monitoring and personal health management.

3. Conclusions

In summary, we propose a conformal self-powered inertial displacement sensor featuring geometric optimization for in situ noninvasive data acquisition. Employing template-assisted processing and COMSOL simulation, we have discerned specific geometric configurations that exhibit inherent advantages in monitoring human body sensing applications. The curvature of the semicylindrical configuration maximizes contact surface area, enhancing CSIDS signals and enabling superior monitoring of joint range of motion compared to alternative configurations. These findings underscore the crucial role of geometric configurations in tribo-layer materials for optimizing the sensing capabilities of triboelectric nanogenerator-based motion sensors. A carbon doped Ecoflex layer functions as a protective barrier between the joint skin and CSIDS, ensuring heightened reliability in identification. Integration of a deep learning model based on MLP networks, adept at capturing the features of shoulder joint bending angles and humeral linear accelerations, achieves an average accuracy of 99.38% and 99.58%. Furthermore, owing to the outstanding ductility of CSIDS, it maintains a robust linear relationship between triboelectric signals and applied strain at 110%, enabling prolonged surveillance of shoulder motion. Demonstrations include monitoring wrist and elbow joint movements. Monitoring the shoulder joint bend angle and humeral linear acceleration provided a comprehensive assessment of upper limb joint health. The range of motion in the shoulder joint and the load on the humerus were critical aspects of joint health. By integrating these two types of data, a more complete understanding of joint health and potential issues was achieved.

4. Experimental Section

Fabrication of the CSIDS: Liquid Ecoflex rubber was obtained by mixing the Ecoflex base and curing it in a volume ratio of 1:1 (Ecoflex supersoft Ecoflex 0030, Smooth-On, Inc, PA, USA) in a beaker. Carbon blacks were then added to the beaker and stirred to obtain a uniform conductive Ecoflex. The volume ratio of carbon blacks to Ecoflex was 1:15. this method involved constructing a hemisphere mold body using 3D modeling software, followed by 3D printing with polylactic acid (PLA). During the process of hot melt extrusion, PLA formed a textured structure of surface stripes. Subsequently, Ecoflex materials A and B were mixed and poured into the 3D mold to achieve the initial preparation of CSIDS. After the Ecoflex semi-solidified, the residual part of the mold with carbon-doped Ecoflex was filled to form the main structure of CSIDS. Based on this, Ecoflex and carbon-doped Ecoflex were further deposited to form the insulating layer and shielding layer. Finally, the mold was placed in a vacuum drying oven for drying. After 5 h, the mold was removed for demolding.

Electric Measurement and Characterization: A linear motor was used to create alternative motions, and a programmable electrometer (Keithley 6514) and a data acquisition card (NI-6259) were used to measure the output voltage. The software platform was constructed based on LabVIEW for realizing in situ data acquisition.

Supporting Information

Supporting Information is available from the Wiley Online Library or from the author.

Acknowledgements

This work was supported by the Beijing Natural Science Foundation (Grant No. IS23040), the Beijing Municipal Health Commission (BJRITO-RDP-2024) and the Innovation Team Program of Jinan City (Grant No. 202333029). The authors thank Shaoxin Li, Xiang Li, Yu Wei and Yaowen Ouyang from the Beijing Institute of Nanoenergy and Nanosystems for their help in checking the manuscript, building experimental platforms, and shooting demonstration videos.

Conflict of Interest

The authors declare no conflict of interest.

Author Contributions

D.W. and Z.L.W. proposed the idea and the project. D.W. designed all the experiments and supervised the whole project. Y.D. carried out the experiments in this paper. P.H.S., H.F.L., and T.L.R. provided support for the data algorithm. Z.W.Z. provided support for theoretical simulations. R.S. provided basic information on bone and joints. Y.D. and P.H.S. analyzed the corresponding data. All the authors discussed the results and commented on the manuscript. D.W. and Y.D. wrote this paper.

Data Availability Statement

The data that support the findings of this study are available from the corresponding author upon reasonable request.

Keywords

conformal and self-powered sensor, geometric optimization, in situ monitoring, noninvasive data acquisition, triboelectric nanogenerator

Received: June 3, 2024
Revised: August 9, 2024
Published online: August 19, 2024

[1] a) C. A. Kennedy, B. C. Amick 3rd, J. T. Dennerlein, S. Brewer, S. Catli, R. Williams, C. Serra, F. Gerr, E. Irvin, Q. Mahood, A. Franzblau, D. Van Eerd, B. Evanoff, D. Rempel, *J. Occup. Rehabil.* **2010**, *20*, 127; b) D. A.-O. Salvagioni, F. N. Melanda, A. E. Mesas, A. D. GonzÃ¡lez, F. L. Gabani, S. A.-O. Andrade, *PLoS One* **2017**, *12*, 0185781.

[2] D. Jun, M. Zoe, V. Johnston, S. O'Leary, *Int. Arch. Occup. Environ. Health.* **2017**, *90*, 373.
[3] a) K. R. Westerterp, *Intl. J. Obesity* **1999**, *23*, S45; b) Y.-S. Lu, H.-W. Wang, S.-H. Liu, *Measurement* **2018**, *125*, 471.
[4] a) H. J. Luinge, P. H. Veltink, *Medical Biol. Eng. Comput.* **2005**, *43*, 273; b) I. Koo, Y. Park, M. Jeong, C. Kim, *IEEE Sens. J.* **2023**, *23*, 506.
[5] a) N. Lu, C. Lu, S. Yang, J. Rogers, *Adv. Funct. Mater.* **2012**, *22*, 4044; b) S. J. Hoshaw, D. P. Fyhrie, Y. Takano, D. B. Burr, C. Milgrom, *J. Biomech.* **1997**, *30*, 521.
[6] a) F. Baldini, A. G. Mignani, *MRS Bull.* **2002**, *27*, 383; b) H. Ai, N. Michiko, C. Yongwoon, W. Kazuhiro, presented at *Proc. SPIE*, **2011**.
[7] a) D. Son, J. Lee, S. Qiao, R. Ghaffari, J. Kim, J. E. Lee, C. Song, S. J. Kim, D. J. Lee, S. W. Jun, S. Yang, M. Park, J. Shin, K. Do, M. Lee, K. Kang, C. S. Hwang, N. Lu, T. Hyeon, D.-H. Kim, *Nat. Nanotechnol.* **2014**, *9*, 397; b) S. Sharma, A. Chhetry, M. Sharifuzzaman, H. Yoon, J. Y. Park, *ACS Appl. Mater. Interfaces* **2020**, *12*, 22212; c) X. Wang, Y. Gu, Z. Xiong, Z. Cui, T. Zhang, *Adv. Mater.* **2014**, *26*, 1336.
[8] a) Q. Hua, J. Sun, H. Liu, R. Bao, R. Yu, J. Zhai, C. Pan, Z. L. Wang, *Nat. Commun.* **2018**, *9*, 244; b) T. Q. Trung, N.-E. Lee, *Adv. Mater.* **2016**, *28*, 4338; c) J. Luo, S. Gao, H. Luo, L. Wang, X. Huang, Z. Guo, X. Lai, L. Lin, R. K. Y. Li, J. Gao, *Chem. Eng. J.* **2021**, *406*, 126898.
[9] a) Z. Lin, J. Chen, X. Li, Z. Zhou, K. Meng, W. Wei, J. Yang, Z. L. Wang, *ACS Nano* **2017**, *11*, 8830; b) Y. Khan, A. E. Ostfeld, C. M. Lochner, A. Pierre, A. C. Arias, *Adv. Mater.* **2016**, *28*, 4373; c) X. Wang, Z. Liu, T. Zhang, *Small* **2017**, *13*, 1602790.
[10] a) C. Ning, R. Cheng, Y. Jiang, F. Sheng, J. Yi, S. Shen, Y. Zhang, X. Peng, K. Dong, Z. L. Wang, *ACS Nano* **2022**, *16*, 2811; b) Y. Su, G. Chen, C. Chen, Q. Gong, G. Xie, M. Yao, H. Tai, Y. Jiang, J. Chen, *Adv. Mater.* **2021**, *33*, 2101262; c) Y. Pang, J. Jian, T. Tu, Z. Yang, J. Ling, Y. Li, X. Wang, Y. Qiao, H. Tian, Y. Yang, T.-L. Ren, *Biosens. Bioelectron.* **2018**, *116*, 123.
[11] a) L. Pan, A. Chortos, G. Yu, Y. Wang, S. Isaacson, R. Allen, Y. Shi, R. Dauskardt, Z. Bao, *Nat. Commun.* **2014**, *5*, 3002; b) C.-L. Choong, M.-B. Shim, B.-S. Lee, S. Jeon, D.-S. Ko, T.-H. Kang, J. Bae, S. H. Lee, K.-E. Byun, J. Im, Y. J. Jeong, C. E. Park, J.-J. Park, U. I. Chung, *Adv. Mater.* **2014**, *26*, 3451; c) Y. Wang, J. Hao, Z. Huang, G. Zheng, K. Dai, C. Liu, C. Shen, *Carbon* **2018**, *126*, 360.
[12] a) Z. Lei, Q. Wang, S. Sun, W. Zhu, P. Wu, *Adv. Mater.* **2017**, *29*, 1700321; b) K. Meng, X. Xiao, W. Wei, G. Chen, A. Nashalian, S. Shen, X. Xiao, J. Chen, *Adv. Mater.* **2022**, *34*, 2109357; c) Z. Wang, Y. Cong, J. Fu, *J. Mater. Chem. B* **2020**, *8*, 3437.
[13] a) L. Persano, C. Dagdeviren, Y. Su, Y. Zhang, S. Girardo, D. Pisignano, Y. Huang, J. A. Rogers, *Nat. Commun.* **2013**, *4*, 1633; b) S. D. Mahapatra, P. C. Mohapatra, A. I. Aria, G. Christie, Y. K. Mishra, S. Hofmann, V. K. Thakur, *Adv. Sci.* **2021**, *8*, 2100864; c) P. Martins, A. C. Lopes, S. Lanceros-Mendez, *Prog. Polym. Sci.* **2014**, *39*, 683.
[14] a) M. Ramuz, B. C. K. Tee, J. B. H. Tok, Z. Bao, *Adv. Mater.* **2012**, *24*, 3223; b) T. Q. Trung, N.-E. Lee, *J. Mater. Chem. C* **2017**, *5*, 2202.
[15] E. Roh, B.-U. Hwang, D. Kim, B.-Y. Kim, N.-E. Lee, *ACS Nano* **2015**, *9*, 6252.
[16] a) Y. Du, S. Fu, C. Shan, H. Wu, W. He, J. Wang, H. Guo, G. Li, Z. Wang, C. Hu, *Adv. Funct. Mater.* **2022**, *32*, 2208783; b) S. Fu, W. He, H. Wu, C. Shan, Y. Du, G. Li, P. Wang, H. Guo, J. Chen, C. Hu, *Nanomicro Lett.* **2022**, *14*, 155; c) Y. Du, Q. Tang, W. He, W. Liu, Z. Wang, H. Wu, G. Li, H. Guo, Z. Li, Y. Peng, C. Hu, *Nano Energy* **2021**, *90*, 106543.
[17] M. Zhong, L. Zhang, X. Liu, Y. Zhou, M. Zhang, Y. Wang, L. Yang, D. Wei, *Chem. Eng. J.* **2021**, *412*, 128649.
[18] a) S. Li, Z. Zhang, F. Yang, X. Li, P. Peng, Y. Du, Q. Zeng, M. Willatzen, Z. L. Wang, D. Wei, *Device* **2024**, *2*, 100332; b) X. Li, S. Li, X. Guo, J. Shao, Z. L. Wang, D. Wei, *Matter* **2023**, *6*, 3912; c) R. Li, D. Wei, Z. Wang, *Nanomaterials (Basel)* **2024**, *14*, 165.
[19] a) M. Khorsand, J. Tavakoli, H. Guan, Y. Tang, *Nano Energy* **2020**, *75*, 104993; b) J. Gravesen, M. Willatzen, J. Shao, Z. L. Wang, *Nano Res.* **2023**, *16*, 11925.
[20] a) S. M. Sohel Rana, O. Faruk, M. Selim Reza, M. Robiul Islam, H. Kim, J. Yeong Park, *Chem. Eng. J.* **2024**, *488*, 151050. b) H. Kim, S. M. S. Rana, M. Robiul Islam, O. Faruk, K. Shrestha, G. B. Pradhan, J. Y. Park, *Chem. Eng. J.* **2024**, *491*, 151980.
[21] S. An, X. Pu, S. Zhou, Y. Wu, G. Li, P. Xing, Y. Zhang, C. Hu, *ACS Nano* **2022**, *16*, 9359.
[22] a) B. Shao, M. H. Lu, T. C. Wu, W. C. Peng, T. Y. Ko, Y. C. Hsiao, J. Y. Chen, B. Sun, R. Liu, Y. C. Lai, *Nat. Commun.* **2024**, *15*, 1238; b) Y. Zhang, X. Zhu, Y. Liu, L. Liu, Q. Xu, H. Liu, W. Wang, L. Chen, *Macromol. Mater. Eng.* **2021**, *306*, 2100113.